GRADUATE AERONAUTICAL LABORATORIES
CALIFORNIA INSTITUTE of TECHNOLOGY
Pasadena, California 91125

Image correlation velocimetry

By P. T. TOKUMARU AND P. E. DIMOTAKIS

Abstract

This paper focuses on the correlation of two successive scalar images for the purpose of measuring imaged fluid motions. A method is presented for deforming, or transforming, one image to another. Taylor series expansions of the Lagrangian displacement field are used, in conjunction with an integral form of the equations of motion, to approximate this transformation. The proposed method locally correlates images for displacements, rotations, deformations, and higher order displacement gradient fields, and applies a global minimization procedure to insure a global consistency in the results. An integral form of the equations of motion is employed and, as a consequence, no spatial or temporal differentiation of the image data is required in estimating the displacement field. Successive two-dimensional digital CCD images of fluid motion marked with dye, are used to verify the capabilities of the method. The utility of the method is also illustrated using a pair of Voyager 2 images of Jupiter.

GALCIT Report FM92–1

20 November 1992

1. Introduction

The application of photographic, CCD, and other forms of imaging for the purpose of estimating flow velocities, has been investigated by many researchers in fields ranging from fluid mechanics to vision research. In the most common methods for measuring fluid flow velocities, the flow is seeded with particles, or markers, that can be easily imaged and tracked. An extensive review of methods using particle and speckle images for fluid flow measurement is presented by Adrian (1991). The estimation of the motion and deformation of solids is closely related to that of fluids. A method of determining displacements and stress intensity factors in solids, using white light speckle images and image correlation techniques, is presented in McNeill *et al.* 1987. In the absence of particles, flows have also been tagged with a line or grid, *e.g.*, using laser-induced photochemical reactions (Falco & Chu 1987), or laser-induced fluorescence (Miles *et al.* 1989). When this is not possible, one can use markers that occur naturally in the flow, *e.g.*, Bindschadler and Scambos (1991) have correlated the translation of distinct surface features in ice flows to determine flow velocities.

Determining motion from successive images is also of interest in animation, as well as the study of biological and robotic vision. Most investigations along these lines have taken the form of extracting the motion of objects in an image and, as a consequence, they focus on the motion of rigid objects and their representations. See Hildreth & Koch (1987) for a review and Murray & Buxton (1990). This approach is somewhat different from the interests of Fluid Mechanics where the object of interest is a fluid, highly deformable and often compressible. Nevertheless, many results from object motion research apply directly to the motion of fluids and solids.

The proposed Image Correlation Velocimetry (ICV) method that will be developed in the present discussion has roots in both the correlation methods used in measuring fluid flow and the deformation of solids, outlined in Sec. 1.1, and the gradient methods used in measuring optical flows, outlined in Sec. 1.2.

1.1 Correlation methods

Several techniques for determining fluid flow velocities from particle image pairs (*e.g.*, Willert & Gharib 1991) employ an optimization that relies on some form of a cross-correlation function, *e.g.*,

$$\max_{\mathbf{a}} \int_A E_0(\mathbf{x})\, E_1(\boldsymbol{\xi})\ \mathrm{d}^2\mathbf{x}\,, \tag{1}$$

with

$$\boldsymbol{\xi} = \mathbf{x} + \mathbf{a}\ , \tag{2}$$

where $\mathbf{a}$ is a vector parameter to be determined by the optimization procedure and A is the correlation region. The distribution of the image irradiance, $E(\mathbf{x},t)$, is known at times t_0 and t_1, *i.e.*,

$$E_0(\mathbf{x}) \equiv E(\mathbf{x},t_0) \qquad \text{and} \qquad E_1(\mathbf{x}) \equiv E(\mathbf{x},t_1) \ . \tag{3}$$

The average velocity, $\mathbf{u}_A$, within the correlation region is then approximated by,

$$\mathbf{u}_A \ \approx \ \frac{\mathbf{a}}{t_1 - t_0} \ . \tag{4}$$

The drawback of this method, having only two parameters to quantify the motion, is that it cannot resolve displacements properly where there are large displacement gradients within the correlation region. Anticipating this problem, and being very interested in displacement gradients, researchers in Solid Mechanics, apply techniques which include higher order deformations of the displacement field within a correlation volume. For example, McNeill *et al.* (1987) describe a method whereby a model of the image displacement field (mapping) is used in a least squares optimization procedure, *i.e.*,

$$\min_{\mathbf{a},\nabla\mathbf{a}} \int_A \ [\, E_0(\mathbf{x}) \ - \ E_1(\xi) \,]^2 \ \ \mathrm{d}^2\mathbf{x} \ . \tag{5}$$

The affine mapping,

$$\xi \ = \ \mathbf{x} + \mathbf{a} + (\nabla\mathbf{a}) \cdot \mathrm{d}\mathbf{x} \ , \tag{6}$$

is used as an example of such a function, and the displacement $\mathbf{a}$ and the four components of $\nabla\mathbf{a}$ are treated as parameters to be determined by the optimization procedure. However, any physically motivated mapping can be used in place of Eq. 6.

In both these methods, the image data are integrated over a region and require no spatial differentiation. Since, for two-dimensional images, only a few parameters are extracted from the optimization, these methods are relatively immune to noise and lend themselves to fast solutions.

1.2 Gradient methods

A method for determining the velocities of visual features in an image was presented by Horn & Schunck (1981). This visual velocity is termed "optical flow" to differentiate it from the velocities of (material) objects in an image, *e.g.*, a shadow moving across the ground has a perceived velocity that is markedly different from that of the ground, and a rotating featureless disk will have no visual velocity at all. The fundamental equation used by Horn & Schunch to determine the optical flow was,

$$\frac{\partial E}{\partial t} + \mathbf{u} \cdot \nabla E \ = \ 0 \ , \tag{7}$$

where E is the image irradiance (a scalar) and $\mathbf{u}$ is the optical flow velocity. The differential terms, $\partial E/\partial t$ and ∇E, can be estimated from the image data and the component of $\mathbf{u}$ along ∇E is calculated using Eq. 7. Methods employing equations of this type are called gradient schemes. Note that no velocity can be calculated using Eq. 7 if there are no features or gradients in the image, *i.e.*, if $\nabla E = 0$. In addition, because Eq. 7 employs only the component of $\mathbf{u}$ along ∇E, velocity components along the equi-scalar contours of E cannot be determined using Eq. 7 alone. This limitation was designated the "aperture problem" by Wallach (1976). The terminology is somewhat misleading and is only used here in reference to the convention. More appropriate names might be the "characteristic problem," or the "direction problem," because the problem is finding the velocity along the characteristic direction, E = constant. Gradient schemes also have the problem that finite difference approximations of the spatial and temporal derivatives are necessary. A problem with such approximations for the derivatives is related to the Nyquist sampling criterion, where aliasing in the image data can effect the velocity estimates. To minimize this problem in taking the gradient, the motion between images should be less than half the smallest local spatial scale, λ_E, of the $E-$field, *i.e.*,

$$\frac{|\mathbf{u}|\ (t_1 - t_0)}{\lambda_E} < \frac{1}{2} \tag{8}$$

(*cf.* Eq. 7), where $(t_1 - t_0)$ is the time between images.

The uncertainty of the so-called aperture problem can be solved in some cases by applying constraints to the motion, *e.g.*, the motion is of a rigid body (see Murray & Buxton 1990, for example), or a limited class of deformable bodies (see Terzopoulos & Metaxas 1991).

Horn & Schunck (1981) applied a global constraint to Eq. 7 (in two dimensions), by solving for $\mathbf{u}(\mathbf{x}, t)$ using an optimization, *i.e.*,

$$\min_{\mathbf{u}(\mathbf{x},t)} \int_A \left(\left[\frac{\partial E}{\partial t} + \mathbf{u} \cdot \nabla E \right]^2 + k\sigma^2 \right) \mathrm{d}^2\mathbf{x}\,, \tag{9}$$

where σ represents the constraint cost function in the optimization process, and k balances the relative cost of σ and Eq. 7. In particular, Horn & Schunck chose smoothness as a constraint, *i.e.*,

$$\sigma^2 = \sum_{i,j=1,2} \left(\frac{\partial u_i}{\partial x_j} \right)^2 . \tag{10}$$

The idea of including constraints in the optimization process that determines the velocity field, over an area, is important in the context of the method to be discussed below. Note that the constraint in Eq. 9 need not be included in the optimization integral. Instead, it could be included as a feature of the optimization technique. See Murray & Buxton (1990).

2. Proposed methodology

A succession of images can represent anything from the motion of cars on a highway to the transport of a dye marker in water. We take the view that given successive image representations, there exists a transformation, or mapping, of the local image intensity data that takes one image to the next. In many cases, while the equation of motion of the imaged field may be known, the mapping taking one image to another may not be. Successive images combined with the equations of motion, however, often allow us to approximate the mapping.

The mapping of one image to the next can be developed by considering the Lagrangian displacement field $\boldsymbol{\xi}(\mathbf{x},t)$ of the image sequence. Specifically, if $\mathbf{x}$ is the coordinate of a point on an image at some initial time t_0, $\boldsymbol{\xi}(\mathbf{x},t)$ represents the coordinate of this point in a subsequent image recorded at a later time t. If we imagine the image sequence as the result of a continuous recording process, we can assign a Lagrangian *image*-flow velocity field, referred to as "optical flow" in the discussion and literature cited above, *i.e.*,

$$\mathbf{u}[\boldsymbol{\xi}(\mathbf{x},t),t] \;=\; \frac{\mathrm{d}}{\mathrm{d}t}\boldsymbol{\xi}(\mathbf{x},t) \;\;, \tag{11}$$

to the continuous displacement field $\boldsymbol{\xi}(\mathbf{x},t)$ that takes an initial point $\mathbf{x}$ in the image recorded at time t_0, to the point $\boldsymbol{\xi}(\mathbf{x},t)$ on the image recorded at time t. We recognize that, for the case where the images represent fluid flow, *e.g.*, successive images of a convected scalar, the image-flow velocity field, $\mathbf{u}(\mathbf{x},t)$, may be quite different from the *fluid*-flow velocity field $\mathbf{u}_{\mathrm{f}}(\mathbf{x},t)$. The extent to which the former represents a good approximation for the latter is a separate issue that can only be addressed in the context of the details of the particular imaging process and the fluid-flow field.

In the proposed implementation, local series approximations for the displacement mapping are used in conjunction with an integral form of the equations of motion. A global nonlinear correlation (optimization) process is employed to estimate the image-flow velocity, vorticity, deformation rate, *etc.*, of the imaged data field. "Series," in this discussion, will denote "Taylor series."

In the context of fluid mechanics measurements, we will focus on images of continuous, passive, convected scalars, *e.g.*, dye markers, carried by a fluid. As will be illustrated using a pair of Voyager 2 images of Jupiter (Sec. 5), however, any marker in the flow can be used.

The method will be developed for three dimensions and can yield three-dimensional velocity fields. The method can also obtain two-dimensional velocity fields from images of two-dimensional flows. In a concession to the limitations of typical data acquisition systems today, however, the method will be applied here

to a two-dimensional flow and also to two-dimensional slices of three-dimensional flows. We note that in some cases, two-dimensional imaging devices can be used to obtain approximations to three-dimensional image data, *e.g.*, Dahm, *et al.* 1991. A short discussion of the implications of correlating two-dimensional slices of three-dimensional data is presented in Sec. 4.

2.1 Fluid displacement and equations of motion

To see how the image-flow velocity field can be calculated from three-dimensional image data sets, spaced in time, first consider a Lagrangian description of a flow being imaged. Figure 1 illustrates the motion of fluid particles within a volume, V. Fluid elements at $\mathbf{x}$, in a neighborhood V, at time t_0, are convected to locations $\boldsymbol{\xi}(\mathbf{x},t)$ at a later time t. The displacement field, $\boldsymbol{\xi}(\mathbf{x},t)$, can be thought of as a transformation of the field $\mathbf{x}$, at time t_0, to $\boldsymbol{\xi}(\mathbf{x},t)$. Given the image displacement field $\boldsymbol{\xi}(\mathbf{x},t)$, the image-flow velocity field is then given by Eq. 11.

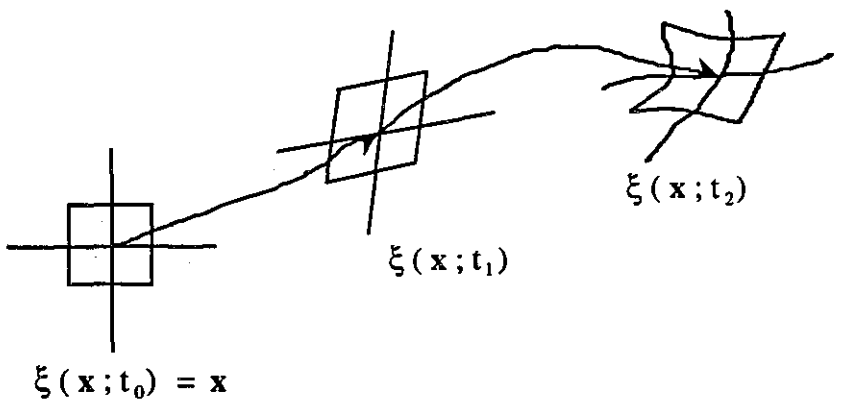

FIG. 1 Motion of a fluid volume.

Using this Lagrangian field, $\boldsymbol{\xi}(\mathbf{x},t)$, one could, in principle, integrate the equation of motion of the imaged scalar, *i.e.*,

$$\frac{\partial c}{\partial t} + \mathbf{u}\cdot\nabla c \;=\; \mathcal{D}\nabla^2 c \;, \tag{12}$$

to obtain

$$c_1\big[\,\boldsymbol{\xi}(\mathbf{x},t_1)\,\big] - c_0\big[\,\boldsymbol{\xi}(\mathbf{x},t_0)\,\big] - \mathcal{D}\int_{t_0}^{t_1} \nabla^2 c\big[\boldsymbol{\xi}(\mathbf{x},\tau),\tau\big]\,\mathrm{d}\tau \;=\; 0 \;, \tag{13}$$

where

$$c_0(\mathbf{x}) \equiv c(\mathbf{x}, t_0) \qquad \text{and} \qquad c_1(\mathbf{x}) \equiv c(\mathbf{x}, t_1) \tag{14}$$

represent the $c(\mathbf{x}, t)$-field at times t_0 and t_1, respectively, and $\mathcal{D}$ is the appropriate diffusion coefficient.

In the first two examples, the motion of food coloring in glycerine (Sec. 3) and dilute fluorescein in water (Sec. 4), are examined. In these flows, the diffusion of the dye markers, in the time interval between successive images, is relatively small and may be neglected, *i.e.*,

$$\frac{(t_1 - t_0)\,\mathcal{D}}{\ell^2} \ll 1 \ , \tag{15}$$

where, $t_1 - t_0 = 0.1$ s is the time between images, $\ell = 50$ to $80\,\mu$m is the imaging resolution, and the diffusion coefficients are no larger than $\mathcal{D} = 10^{-9}\,\mathrm{m}^2/\mathrm{s}$. In addition, we note that the Schmidt number is large in both flows, *i.e.*,

$$S_c \equiv \nu/\mathcal{D} > 10^3 \ , \tag{16}$$

where ν is the kinematic viscosity. In the first example of the dye marker in glycerine, the fluid flow is two-dimensional, as is the image, and the image-flow velocity field, $\mathbf{u}(\mathbf{x}, t)$, is a good representation of the fluid-flow velocity field, $\mathbf{u}_\mathrm{f}(\mathbf{x}, t)$. In the second example, both the flow velocity and the imaged scalar field are three-dimensional, while the image is two-dimensional. As we will discuss, the image-flow field need not necessarily represent the flow velocity field, in that case. In the third example, the motion of the imaged quantity in the Jovian atmosphere (Sec. 5) does not follow any simple equation of motion. In that example, the derived image-flow velocity field can be expected to be an even poorer representation of the fluid-flow velocity field.

In cases where the diffusion of the imaged scalar can be ignored, Eq. 13 becomes

$$c_1\big[\boldsymbol{\xi}(\mathbf{x}, t_1)\big] - c_0\big[\boldsymbol{\xi}(\mathbf{x}, t_0)\big] \ = \ 0 \ . \tag{17}$$

Equation 17 represents a significant simplification over Eq. 12, its differential counterpart. It contains no spatial, or temporal, derivatives and suffers few of the drawbacks associated with the gradient methods discussed earlier (Sec. 1.2).

Using the integral equation of motion (Eq. 17) in place of the differential equation of motion (Eq. 7) in the optimization (Eq. 9), and generalizing the optimization to three dimensions then yields an expression for determining $\boldsymbol{\xi}(\mathbf{x}, t_0)$ and $\boldsymbol{\xi}(\mathbf{x}, t_1)$, *i.e.*,

$$\min_{\boldsymbol{\xi}(\mathbf{x},t_0),\,\boldsymbol{\xi}(\mathbf{x},t_1)} \int_\mathrm{V} \left(\Big\{ c_1\big[\boldsymbol{\xi}(\mathbf{x}, t_1)\big] - c_0\big[\boldsymbol{\xi}(\mathbf{x}, t_0)\big] \Big\}^2 \ + \ k\,\sigma^2 \right) \mathrm{d}^3\mathbf{x} \ . \tag{18}$$

In the spirit of the correlation methods discussed in Sec. 1.1, where the type of motion within the correlation volume is limited to translation alone, the present method restricts $\boldsymbol{\xi}(\mathbf{x}, t_0)$ and $\boldsymbol{\xi}(\mathbf{x}, t_1)$ to the first few terms of a series approximation for $\boldsymbol{\xi}(\mathbf{x}, t)$. While many representations of the displacement field could be employed, a (Taylor) series representation is used because the first two orders in the series expansion correspond to physical fluid mechanical quantities, *i.e.*, the velocity vector and the velocity gradient tensor. More importantly, the series approximation has the additional benefit of enforcing smoothness in the displacement and displacement gradient fields within a correlation volume.

2.2 Displacement field and kinematic quantities

In the case of fluid-flow images, the quantity $\boldsymbol{\xi}(\mathbf{x}, t)$ is a complicated nonlinear function of the imaging process, the nonlinear convection dynamics, and $\mathbf{x}$. Local estimates of this function can be made by Taylor series, expanding $\boldsymbol{\xi}(\mathbf{x}, t)$ in space, at some time t, in an image correlation volume, V. This yields,

$$\boldsymbol{\xi}(\mathbf{x}, t) = \boldsymbol{\xi}(\mathbf{x}_c; t) + (\mathbf{x} - \mathbf{x}_c) \cdot \nabla \boldsymbol{\xi}(\mathbf{x}_c; t) + \frac{1}{2!} \left[(\mathbf{x} - \mathbf{x}_c) \cdot \nabla\right]^2 \boldsymbol{\xi}(\mathbf{x}_c; t) + \ldots \qquad (19)$$

In this expression, $\mathbf{x}_c$ denotes the center of the image correlation volume, V, at time t_0, and $\nabla \boldsymbol{\xi}(\mathbf{x}_c; t)$ denotes the gradient of $\boldsymbol{\xi}(\mathbf{x}, t)$ with respect to $\mathbf{x}$, evaluated at $\mathbf{x}_c$. Figure 2 plots the number of parameters used in the optimization process as a function of the order used in the series expansion, for two and three dimensions. Figure 3 illustrates the effect of the various orders of the expansion on a two-dimensional square "volume."

Using a finite difference approximation in time for the velocity, Eq. 11, and the series representation, Eq. 19, evaluated at times t_0 and t_1, yields an estimate for the velocity within the correlation volume, *i.e.*,

$$\mathbf{u}\left[\boldsymbol{\xi}(\mathbf{x}; t), t\right] \simeq \frac{\boldsymbol{\xi}(\mathbf{x}; t_1) - \boldsymbol{\xi}(\mathbf{x}; t_0)}{t_1 - t_0} \qquad (20)$$

where $t_0 \leq t \leq t_1$. Similarly, taking the spatial gradient of Eq. 20 yields an expression for the velocity gradient tensor within the correlation volume, *i.e.*,

$$\nabla \mathbf{u}\left[\boldsymbol{\xi}(\mathbf{x}; t), t\right] \equiv \frac{\partial}{\partial \mathbf{x}} \mathbf{u}\left[\boldsymbol{\xi}(\mathbf{x}; t), t\right] \simeq \frac{\nabla \boldsymbol{\xi}(\mathbf{x}; t_1) - \nabla \boldsymbol{\xi}(\mathbf{x}; t_0)}{t_1 - t_0} \; . \qquad (21)$$

Vorticity, divergence, and strain rate can then be obtained from the components of the estimated velocity gradient tensor, Eq. 21.

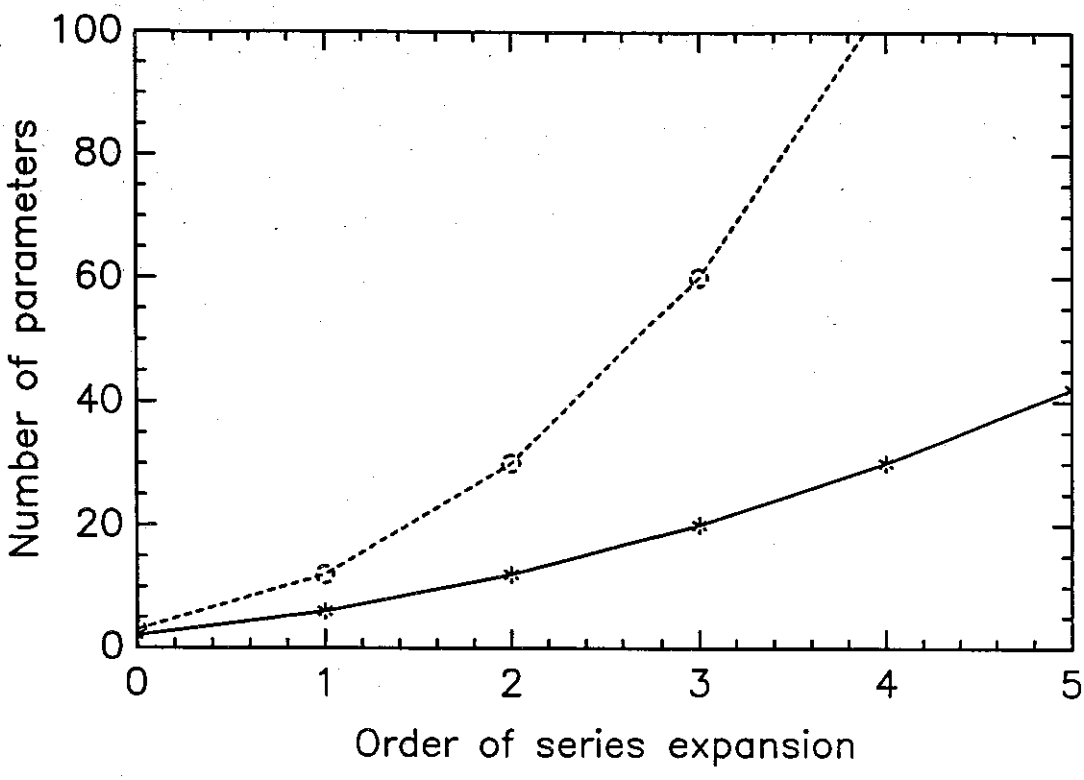

FIG. 2 This plot shows the rapid increase in the number of parameters used in the optimization procedure with increasing order of the series expansion. "$*$" is for a 2-D expansion and"o" for 3-D.

There is some freedom in choosing the coordinate transformation at the initial time t_0, $\boldsymbol{\xi}(\mathbf{x}, t_0)$. Our choice is to have the coordinate description at the initial time t_0 correspond with the local Eulerian coordinates at that time, *i.e.*,

$$\boldsymbol{\xi}(\mathbf{x}, t_0) = \mathbf{x} \ . \tag{22}$$

In terms of the series expansion, Eq. 19, this means that

$$\nabla \boldsymbol{\xi}(\mathbf{x}_c; t_0) \equiv \mathbf{I} \ , \tag{23}$$

where $\mathbf{I}$ is the identity tensor, and all other higher order derivative terms are identically zero.

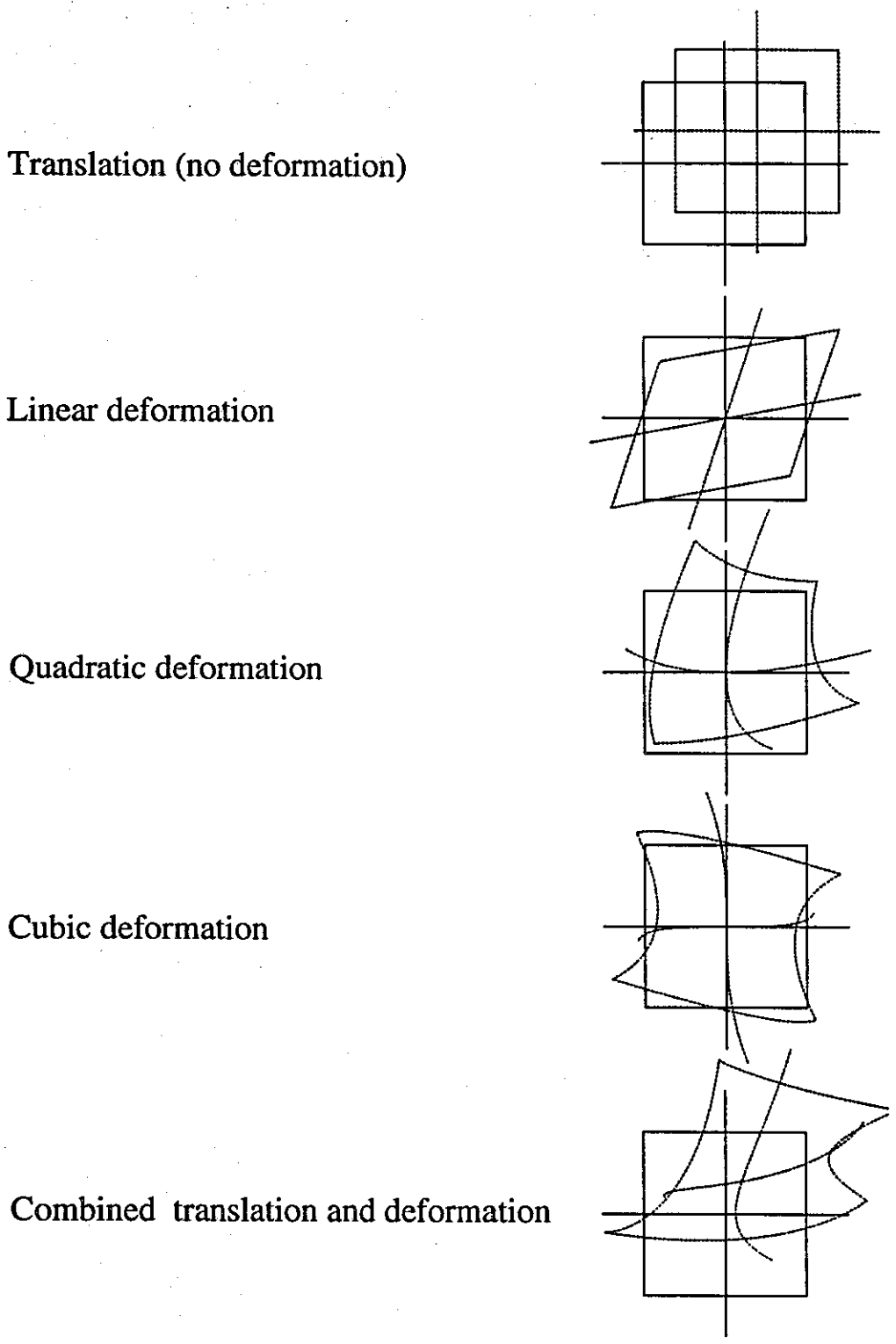

FIG. 3 The effect if translation and various orders of deformation on a two-dimensional square "volume." See Sec. 2.2.

2.3 Seeking a global solution

A solution for the coefficients of the series expansion, *i.e.*, $\xi(\mathbf{x}_c;t)$, $\nabla\xi(\mathbf{x}_c;t)$, *etc.*, can be obtained in a neighborhood around $\mathbf{x}_c$ using the expansions for $\xi(\mathbf{x},t_0)$ and $\xi(\mathbf{x},t)$ from Sec. 2.2. The unknown coefficients of the series expansion, $\xi(\mathbf{x}_c;t)$, $\nabla\xi(\mathbf{x}_c;t)$, *etc.*, are treated as parameters in an optimization process. To minimize the difference between two data sets (images), in a least squares sense, for a single correlation volume, we use the optimization, Eq. 18, in conjunction with the series approximations developed in Sec. 2.2, *i.e.*,

$$\min_{\xi(\mathbf{x}_c;t_1),\nabla\xi(\mathbf{x}_c;t_1),\ldots}\int_V\left(\left\{c_1\left[\xi(\mathbf{x}_c;t_1)+(\mathbf{x}-\mathbf{x}_c)\cdot\nabla\xi(\mathbf{x}_c;t_1)+\ldots\right]-c_0[\mathbf{x}]\right\}^2+\right.$$

$$\left.+\;k\sigma^2\right)\;\mathrm{d}^3\mathbf{x}\;. \tag{24}$$

The optimization implied in Eq. 24, combines many of the best features of correlation methods and gradient methods, while eliminating many of the deficiencies. Specifically, this optimization method has high immunity to noise, uses the equations of motion, can incorporate constraints, requires no differentiation to calculate the displacement field, and can capture displacement gradients within a correlation volume.

In principle, a single correlation volume covering the entire image and a series approximation of a high enough order can be used to capture the entire image displacement field. In practice, however, employing a series approximation beyond the third order (cubic) term is impractical because of the rapid increase in the number of parameters in the optimization process with increasing order (see Fig. 2), and the associated increase in the computational time and complexity. In the present calculations, when the quadratic term is not sufficient to capture the image deformation over the entire flow field using a single volume, as is usually the case, several series expansions residing in smaller, adjacent, correlation volumes are used in place of the single large volume.

To construct a global optimization using a number of local series expansions, we require that neighboring correlation volumes, with independent series expansions, must yield consistent results. In the present method, we use the expansion for the displacement field about one correlation volume to estimate those of its neighbors. The displacement field of these neighbors is also estimated in terms of their own series expansions. The root-mean-square difference between displacements estimated by neighboring correlation volumes is applied as a constraint cost function. Since it is necessary to refer to a number of series expansions, it is useful to define the

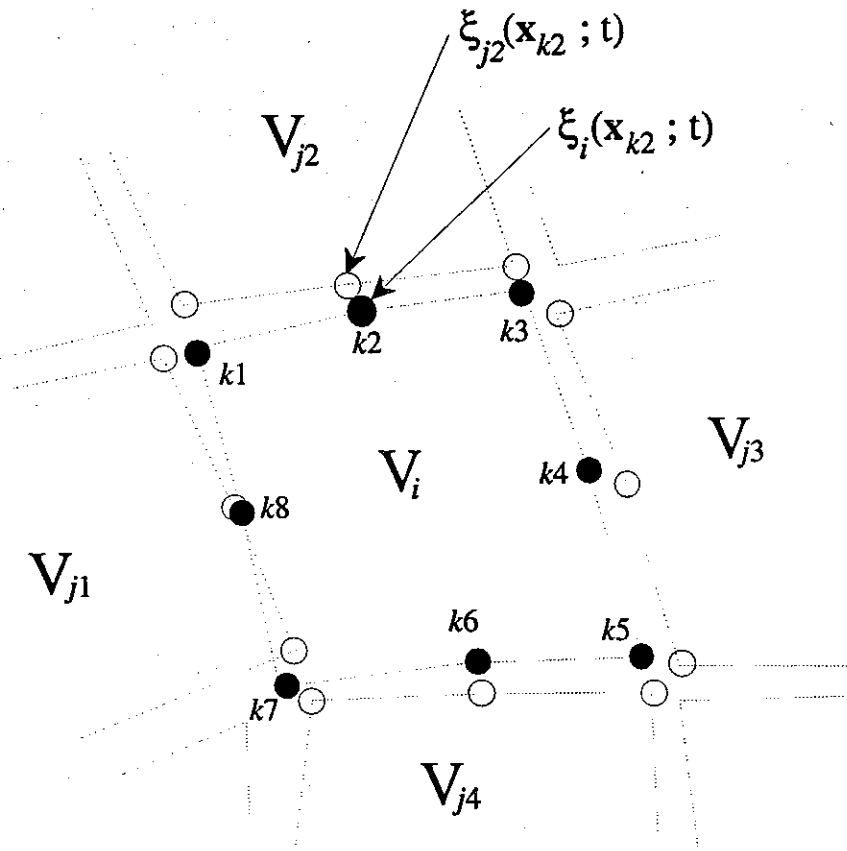

FIG. 4 The $k1$ - $k8$ solid circles denote the points in V_i used by the constraint cost function σ_i. The empty circles denote their counterparts estimated by the neighbors V_{j1} - V_{j4}.

taylor series for $\xi(\mathbf{x},t)$ in a neighborhood V_i centered about $\mathbf{x}_{c_i}$, as

$$\xi_i(\mathbf{x};t) \equiv \xi(\mathbf{x}_{c_i};t)+(\mathbf{x}-\mathbf{x}_{c_i})\cdot\nabla\xi(\mathbf{x}_{c_i};t)+\frac{1}{2!}\left[(\mathbf{x}-\mathbf{x}_{c_i})\cdot\nabla\right]^2\xi(\mathbf{x}_{c_i};t)+\ldots \quad . \quad (25)$$

When series expansions about multiple points are then employed, the minimization, Eq. 24, is modified, *i.e.*,

$$\min_{\xi(\mathbf{x}_{c_i};t_1),\nabla\xi(\mathbf{x}_{c_i};t_1),\ldots}\int_{V_i}\left(\left\{c_1\left[\xi_i(\mathbf{x};t_1)\right]-c_0[\mathbf{x}]\right\}^2+\;k\,\sigma_i^2\right)\;\mathrm{d}^3\mathbf{x}\;,\;\forall i\;. \quad (26)$$

This minimization is performed within all the V_i, simultaneously, and the square of the constraint cost function,

$$\sigma_i^2 \;=\; \sum_j\sum_k\left|\,\xi_i(\mathbf{x}_k;t)-\xi_j(\mathbf{x}_k;t)\,\right|^2 \quad (27)$$

is applied to provide global continuity of the solution. ξ_j denotes the series expansion about the "j" neighbors of V_i, and $\mathbf{x}_k$ denotes the "k" points of comparison between the solutions ξ_i and ξ_j. See Fig. 4. In the present method, eight points about each correlation volume are used for comparison, three with each of four neighbors. These eight points are sufficient to define the series expansion coefficients of the correlation volume, up to quadratic order.

The present implementation of the method can solve Eq. 26 for two-dimensional flow up to the cubic term in the local series expansions, but the series is usually truncated at quadratic order. The optimization of Eq. 24 is accomplished using a multidimensional minimization process, with image data between pixels estimated using bilinear interpolation. See for example Press, *et al.* (1988).

2.4 Minimization parameters in two dimensions

Typical CCD imaging technologies today are limited to two-dimensional (spatial) data. This is not a problem if the flow being imaged is also two-dimensional. This section describes how the method is applied in two dimensions. First, we develop the terms of the series expansion, Eq. 19, for two-dimensional flow. With the two-dimensional vector

$$\begin{bmatrix} \delta_1 \\ \delta_2 \end{bmatrix} \equiv \mathbf{x} - \mathbf{x}_c \ , \tag{28}$$

as the position, $\mathbf{x}$, relative to the center of the correlation volume, $\mathbf{x}_c$, the terms of the series expansion at a time t_1 appear as a constant term,

$$\xi(\mathbf{x}_c; t_1) = \begin{bmatrix} \alpha_1 \\ \alpha_0 \end{bmatrix} \ , \tag{29}$$

where the α_i are the vector coordinates of the center of the correlation volume at the time t_1, *i.e.*,

$$\alpha_i \equiv \xi_i(\mathbf{x}_c; t_1) \ , \tag{30}$$

a linear term,

$$(\mathbf{x} - \mathbf{x}_c) \cdot \nabla \xi(\mathbf{x}_c; t_1) = \begin{bmatrix} \alpha_{1,1} & \alpha_{1,2} \\ \alpha_{2,1} & \alpha_{2,2} \end{bmatrix} \cdot \begin{bmatrix} \delta_1 \\ \delta_2 \end{bmatrix} \ , \tag{31}$$

where the $\alpha_{i,j}$ represent the first order deformations and rotations of the image field within the correlation volume, *i.e.*,

$$\alpha_{i,j} \equiv \frac{\partial \xi_i(\mathbf{x}_c; t_1)}{\partial x_j} \ , \tag{32}$$

a quadratic term,

$$\frac{1}{2!} \left[(\mathbf{x} - \mathbf{x}_c) \cdot \nabla \right]^2 \xi(\mathbf{x}_c; t_1) = \begin{bmatrix} \alpha_{1,11} & \alpha_{1,12} & \alpha_{1,22} \\ \alpha_{2,11} & \alpha_{2,12} & \alpha_{2,22} \end{bmatrix} \cdot \begin{bmatrix} \delta_1^2 \\ \delta_1 \delta_2 \\ \delta_2^2 \end{bmatrix} \ , \tag{33}$$

where

$$\alpha_{i,jk} \equiv \frac{1}{2!}\binom{2}{j+k-2}\frac{\partial^2 \xi_i(\mathbf{x}_c;t_1)}{\partial x_j \partial x_k} \quad , \tag{34}$$

a cubic term,

$$\frac{1}{3!}\left[(\mathbf{x}-\mathbf{x}_c)\cdot\nabla\right]^3 \boldsymbol{\xi}(\mathbf{x}_c;t_1) = \begin{bmatrix} \alpha_{1,111} & \alpha_{1,112} & \alpha_{1,122} & \alpha_{1,222} \\ \alpha_{2,111} & \alpha_{2,112} & \alpha_{2,122} & \alpha_{2,222} \end{bmatrix} \cdot \begin{bmatrix} \delta_1^3 \\ \delta_1^2\delta_2 \\ \delta_1\delta_2^2 \\ \delta_2^3 \end{bmatrix} \quad , \tag{35}$$

with

$$\alpha_{i,jkl} \equiv \frac{1}{3!}\binom{3}{i+j+k-3}\frac{\partial^3 \xi_i(\mathbf{x}_c;t_1)}{\partial x_j \partial x_k \partial x_l} \quad , \tag{36}$$

and so on for higher order terms. The $\alpha_{i,jk}$ and $\alpha_{i,jkl}$ are, respectively, related to the second and third derivatives of the displacement field within the correlation volume, *i.e.*, by Eqs. 34 and 36.

The velocity and velocity gradient (Eqs. 20 and 21), can also be written in terms of the parameters of Eqs. 29 and 31 and the series expansions at times t_0 and t_1, *i.e.*,

$$\mathbf{u}(\mathbf{x}_c,t) \equiv \begin{bmatrix} u \\ v \end{bmatrix} = \frac{1}{t_1-t_0}\begin{bmatrix} \alpha_1 - x_c \\ \alpha_2 - y_c \end{bmatrix} \quad , \tag{37}$$

where

$$\mathbf{x}_c = \begin{bmatrix} x_c \\ y_c \end{bmatrix} \tag{38}$$

and

$$\nabla\mathbf{u}(\mathbf{x}_c,t) \equiv \begin{bmatrix} \partial u/\partial x & \partial u/\partial y \\ \partial v/\partial x & \partial v/\partial y \end{bmatrix} = \frac{1}{t_1-t_0}\begin{bmatrix} \alpha_{1,1}-1 & \alpha_{1,2} \\ \alpha_{2,1} & \alpha_{2,2}-1 \end{bmatrix} \quad . \tag{39}$$

Alternatively, the velocity gradient can be written in terms of the in-plane vorticity and rate-of-strain tensor, *i.e.*,

$$\nabla\mathbf{u}(\mathbf{x}_c,t) = \begin{bmatrix} 0 & -\omega_z/2 \\ \omega_z/2 & 0 \end{bmatrix} + \begin{bmatrix} s_{xx} & s_{xy} \\ s_{xy} & s_{yy} \end{bmatrix} \quad , \tag{40}$$

where ω_z is the vorticity, *i.e.*,

$$\omega_z = \frac{\alpha_{2,1}-\alpha_{1,2}}{t_1-t_0} \quad , \tag{41}$$

and s_{xx}, s_{yy}, and s_{xy}, are the components of the rate-of-strain tensor, *i.e.*,

$$s_{xx} = \frac{\alpha_{1,1}-1}{t_1-t_0} \quad , \tag{42}$$

$$s_{yy} = \frac{\alpha_{2,2} - 1}{t_1 - t_0} \ , \tag{43}$$

and

$$s_{xy} = \frac{1}{2} \frac{\alpha_{1,2} + \alpha_{2,1}}{t_1 - t_0} \ . \tag{44}$$

An interesting quantity to consider is the second invariant of the rate-of-strain tensor (see Cantwell 1992, for example), *i.e.*,

$$-2\,q_s \ \equiv \ s_{xx}^2 + 2\,s_{xy}^2 + s_{yy}^2 \ . \tag{45}$$

3. Couette flow between concentric cylinders

An apparatus to generate a Couette flow between concentric cylinders was fabricated for the purpose of testing the method. The cylinders were made from 248 mm lengths of stock Plexiglas tubing. The inner and outer radii of the annular region between the cylinders were nominally 25.2 mm and 40.9 mm. The cylinders were from stock Plexiglas tubing, so the uncertainties in the radii were ± 1 mm. The outer cylinder was rotated with a rotation rate of 1.1 rad/s, with the inner cylinder stationary. In this example, employing a dye marker in glycerine, the fluid flow is nominally two-dimensional and the marker follows the flow. Hence, the image-flow velocity field, $\mathbf{u}$, can be accepted as a good representation of the fluid-flow velocity field, $\mathbf{u}_f$.

Images were recorded using a Texas Instruments Multicam MC-1134GN Multi-Mode B/W Camera. The data were stored digitally using an in-house multiple frame grabber (12-bit A/D), designed by Dan Lang and Paul Dimotakis of GALCIT, set to record up to 28 of the 1134×468 pixel gray level images from the camera, spaced by 100 msec (adjustable between 33 and 267 msec). Because the horizontal and vertical spacing of the pixels were not equal on this CCD, grid spacings and image correlation volumes with a ratio of 1:1.74 (vertical:horizontal pixels) were used to yield a uniform spacing of the data in the real image plane. Flow visualization was performed by randomly distributing red food coloring (dye) on the surface of the fluid. To provide backlighting for the dye marker, the fluid beneath the surface contained a translucent white suspension of 3 μm aluminum oxide (Al_2O_3) particles in glycerine. When illuminated from the side, this provided nearly uniform white backlighting for the dye being imaged on the surface. Because of the depth of field of the imaging and the high density and uniform distribution of the aluminum oxide, scattering from individual particles was not detectable in the video images.

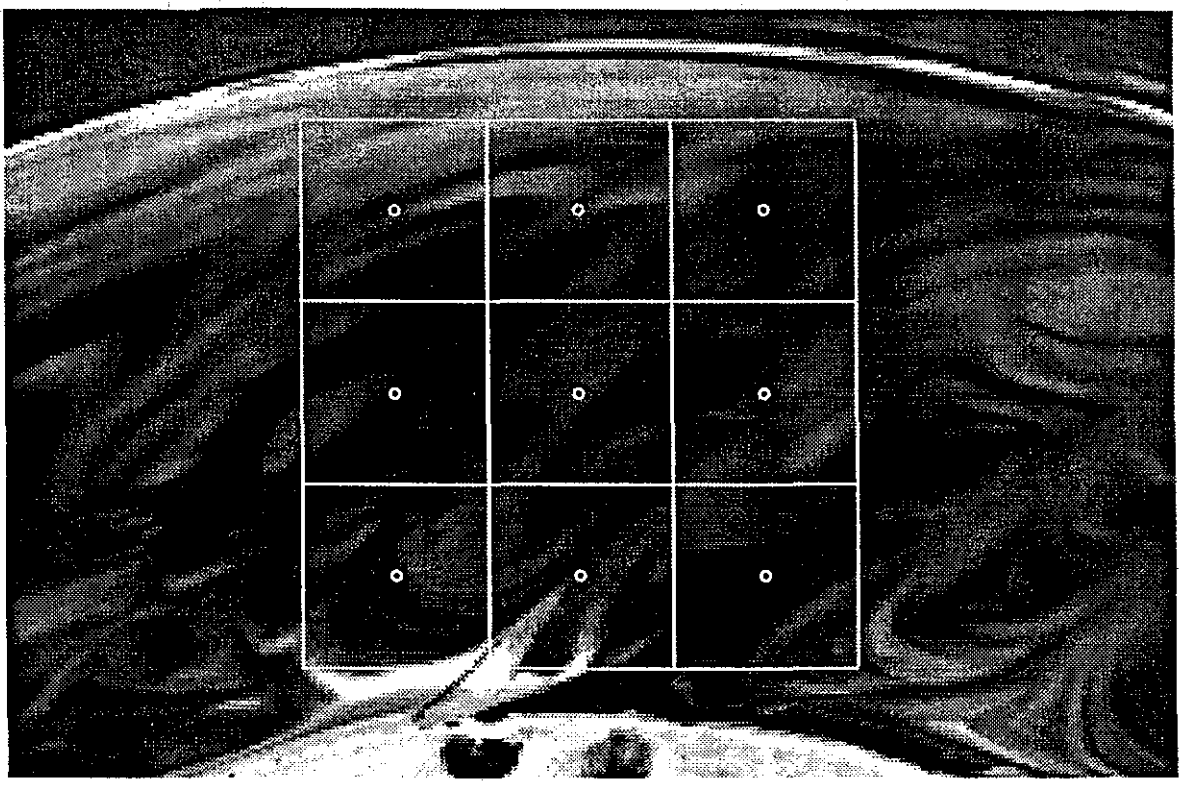

FIG. 5 Initial placement of series expansion neighborhoods. Each square denotes a control volume. The small circle at the center of each control volume denotes the center, or control point, of a series expansion.

In the present investigations, only the outer cylinder was rotated, hence the velocity field can be written as (*e.g.*, Schlichting 1979),

$$\frac{u_r(r,\theta)}{\Omega_o r_o} = 0 \qquad \text{and} \qquad \frac{u_\theta(r,\theta)}{\Omega_o r_o} = \frac{r/r_i - r_i/r}{r_o/r_i - r_i/r_o} \ , \tag{46}$$

where r, θ, u_r, and u_θ are the radial and angular positions and velocities, respectively, Ω_o is the rotation rate of the outer cylinder, and r_i and r_o are the inner and outer radii of the cylinders. In this flow, the divergence is zero, *i.e.*,

$$\nabla \cdot \mathbf{u} = 0 \ , \tag{47}$$

and the vorticity is uniform, *i.e.*,

$$\omega_z(r,\theta) \equiv \mathbf{e}_z \cdot \nabla \times \mathbf{u}(r,\theta) = \frac{2\,\Omega_0}{1-(r_i/r_o)^2} \ . \tag{48}$$

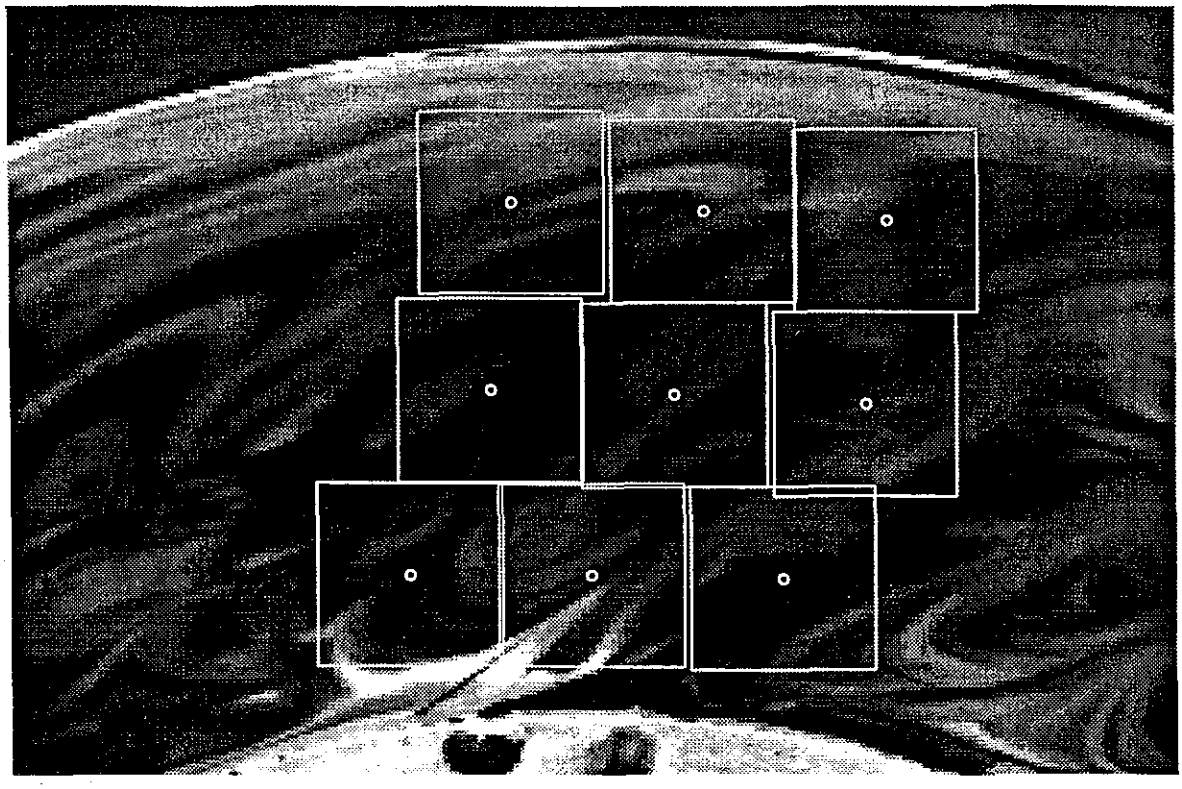

FIG. 6 Displacement of series neighborhoods, 100ms later, allowing only translation.

For this simple test case, nine correlation volumes spaced by 45 pixels vertically and 78.3 pixels horizontally, were used to capture the flow. The locations of the image correlation volumes at the initial time are depicted in Fig. 5. The results of the correlation process, allowing only displacement of the correlation volume (zeroth order series expansion) is shown in Fig. 6. Figure 7 demonstrates how the flow is captured when the correlation process is extended to include higher order terms in the series expansion. To quantify this improvement, the value of the minimization functional, not including the contribution of the constraints, is plotted in Fig. 8 as a function of the order of the series expansion. As can be seen, the greatest improvement is realized with the introduction of linear deformations in the correlation process.

The results using the correlation method are compared with the theoretical (analytical) two-dimensional values for the vorticity and divergence in Table 1. Since both the vorticity and the divergence are uniform in the analytical solution, only a single value is presented. The uncertainty in the theoretical vorticity is a result of the eccentricity of the cylinders used in the experiment. The uncertainties in the experimental values are one standard deviation. Because this flow has a nearly linear velocity profile, we saw only small changes in these estimates, beyond the linear order. Some of the "uncertainty" in the experimental results for the

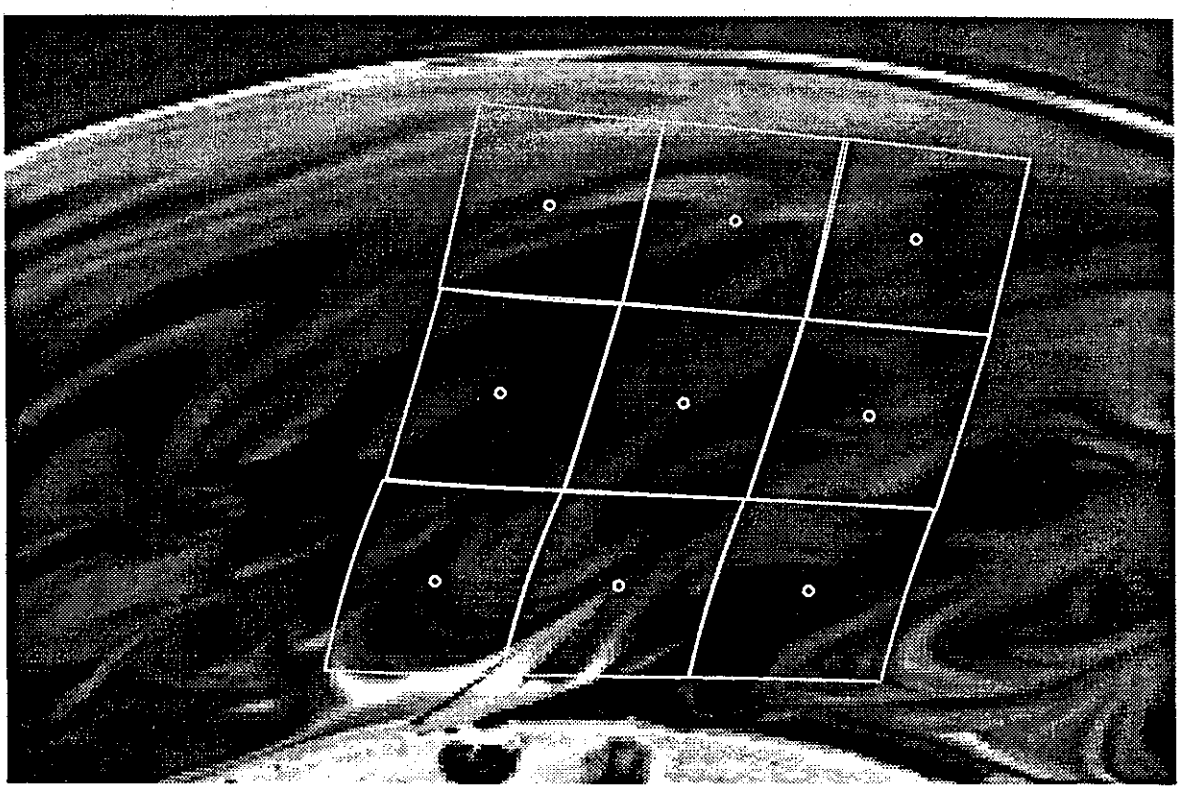

FIG. 7 Displacement of series neighborhoods estimated using higher order terms in the correlation process.

vorticity reflect the expected variations of the vorticity within the flow.

	$\omega_z[\text{sec}^{-1}]$	$\nabla \cdot \mathbf{u}[\text{sec}^{-1}]$
Theoretical:	-3.6 ± 0.1	0.0
Experimental:	-3.6 ± 0.3	-0.1 ± 0.1

TABLE 1. Comparison of theoretical and experimental vorticity and divergence.

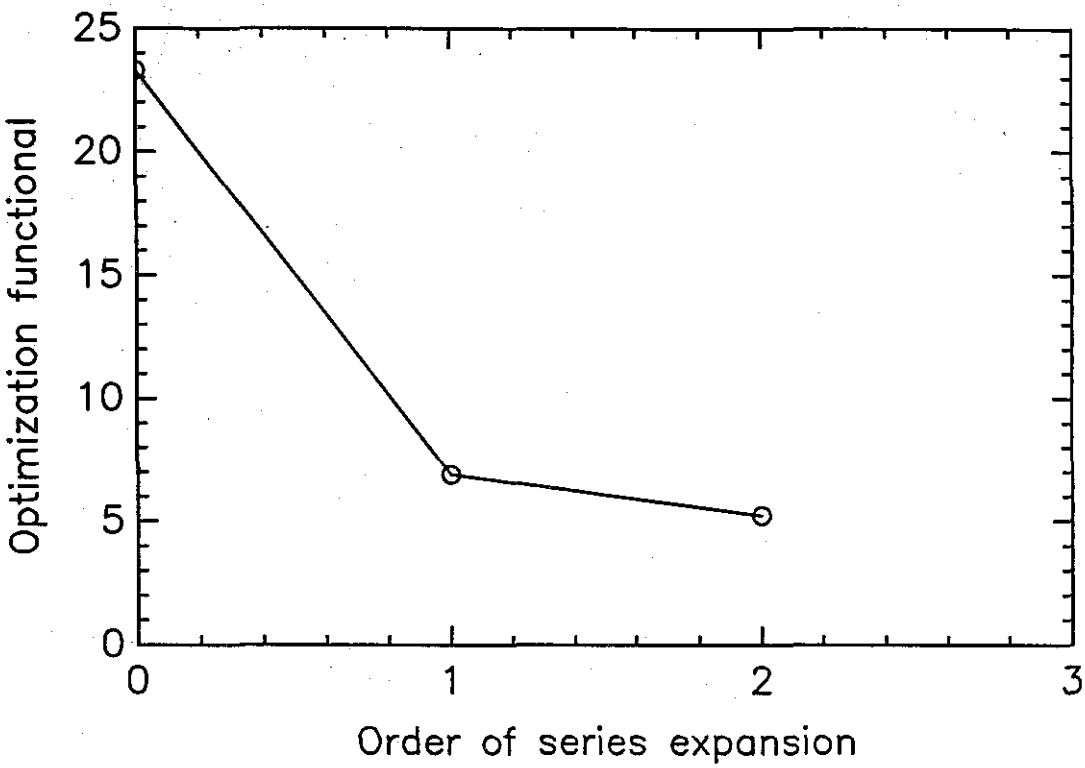

FIG. 8 Difference between Couette flow images under the mapping, quantified by the value of the optimization functional (arbitrary units), as a function of the number of terms in the two-dimensional series expansion.

4. Cylinder wake flow. Two-dimensional slices of three-dimensional data

In this section, we present the results of applying the two-dimensional correlations to two-dimensional slices of a three-dimensional flow in the wake of an impulsively started circular cylinder. Here, the cylinder is 1.75 cm in diameter and 45.5 cm long. It is drawn through a distribution of fluorescein dye in water at a speed of 1.27 cm/s. The Reynolds number in this case is,

$$Re \equiv \frac{U\,d}{\nu} \approx 220 \ , \tag{49}$$

where U is the cylinder speed, d is the cylinder diameter, and ν is the kinematic viscosity.

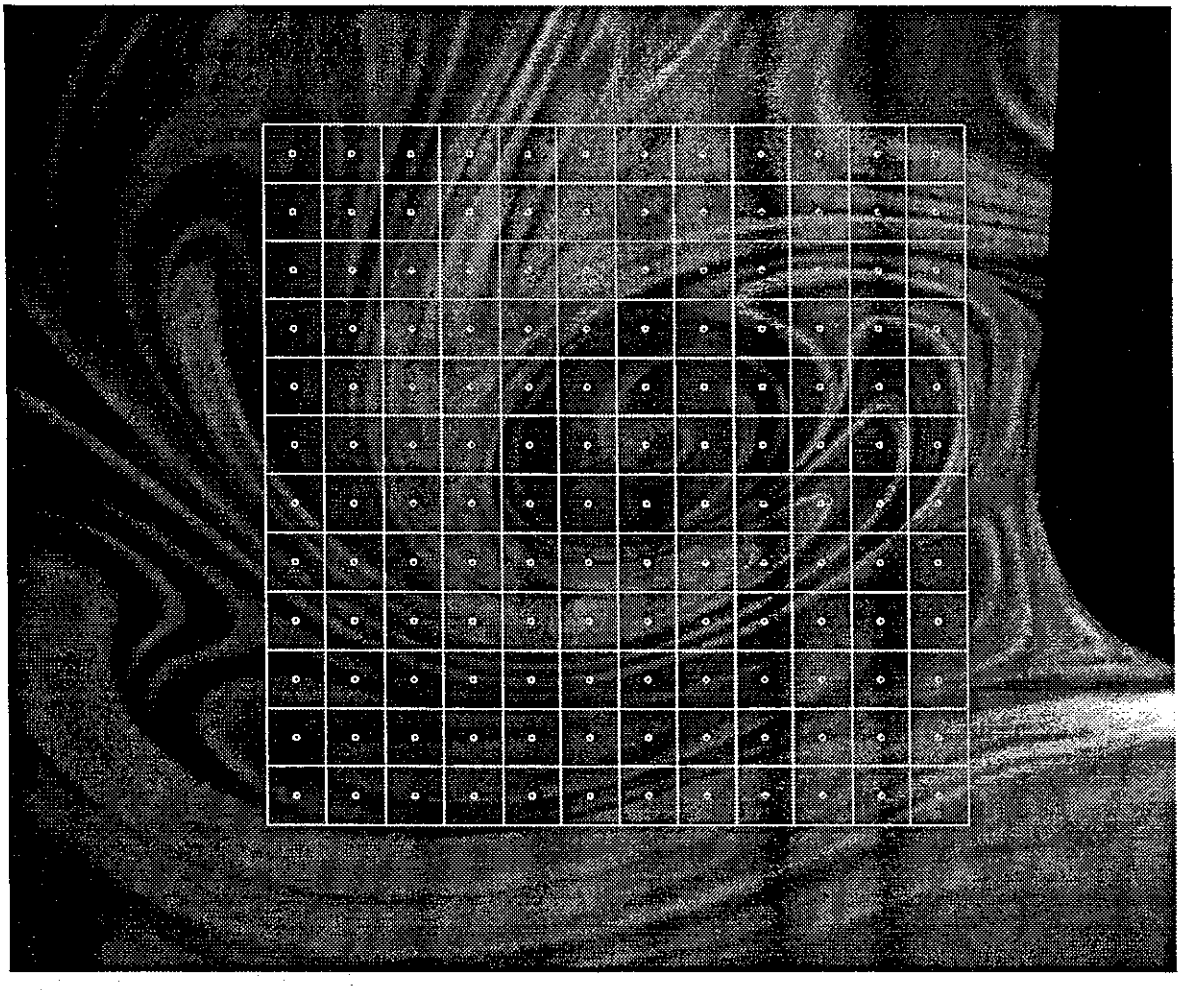

FIG. 9 Initial placement of series expansion neighborhoods. Each square denotes a control volume. The small circle at the center of each control volume denotes the center, or control point, of a series expansion.

The CCD camera and data acquisition system are the same as for the Couette flow test case (Sec. 3). Laser sheet illumination is provided by a Continuum model YG661-10 frequency-doubled YAG laser. The laser was operated at 532 nm, 300 mJ, 5 ns pulses width, at a rate of 10 Hz. The flow here is three-dimensional in both the velocity field and scalar distribution.

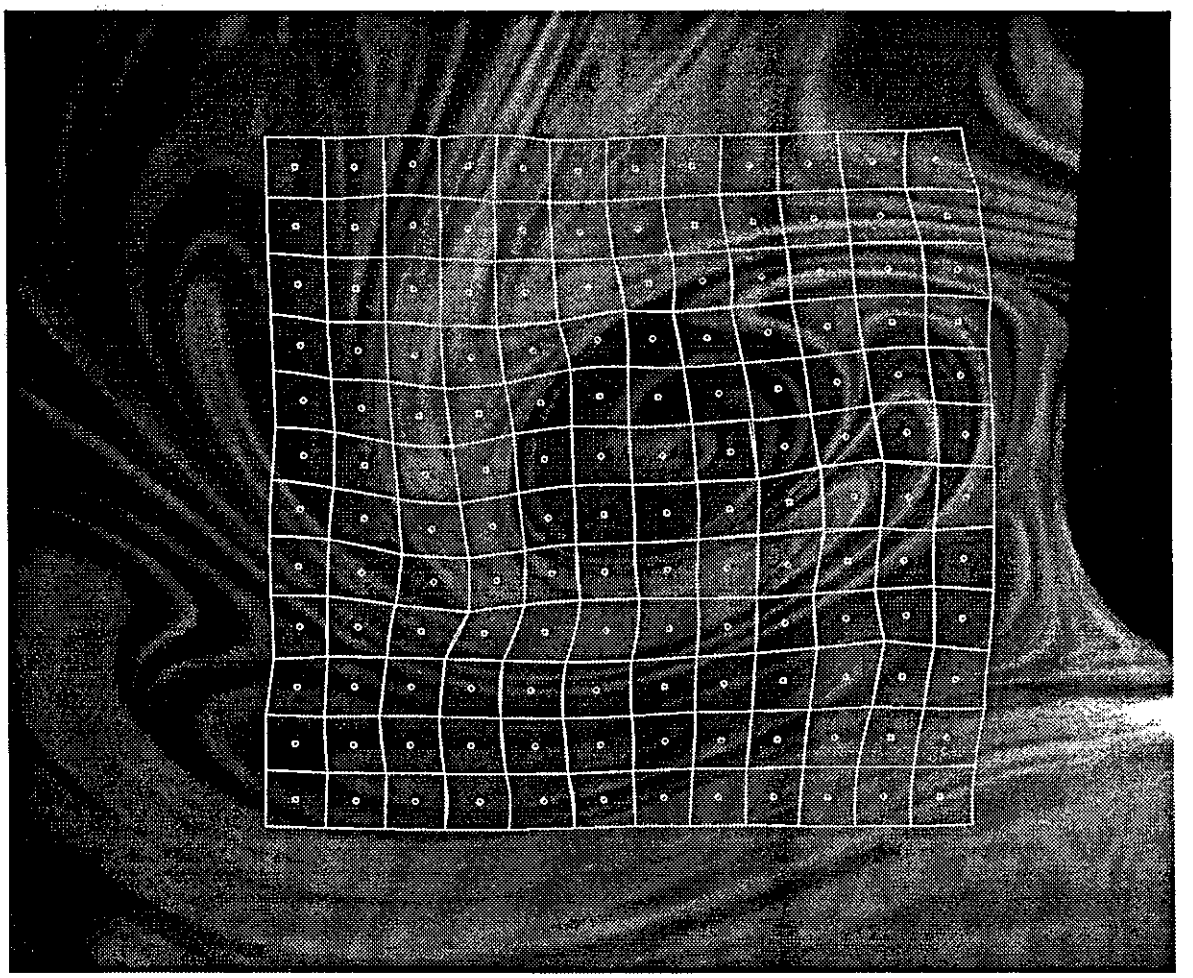

FIG. 10 Displacement of grid after 100 ms, estimated using the nonlinear correlation process.

Figures 9 - 14 demonstrate the method on images of a vortical structure forming in the wake of the cylinder. These images were taken after the cylinder had traveled about 8 diameters. The image at the initial time is shown in Fig. 9, and 100 ms later, in Fig. 10. In this case, the series approximation used in the correlation process was expanded to quadratic order. Figure 11 shows the displacement of the centers of the correlation volumes.

The two-dimensional vorticity is displayed in Fig. 12. A large vortical region can be seen in the wake of the cylinder. The two-dimensional divergence, presented

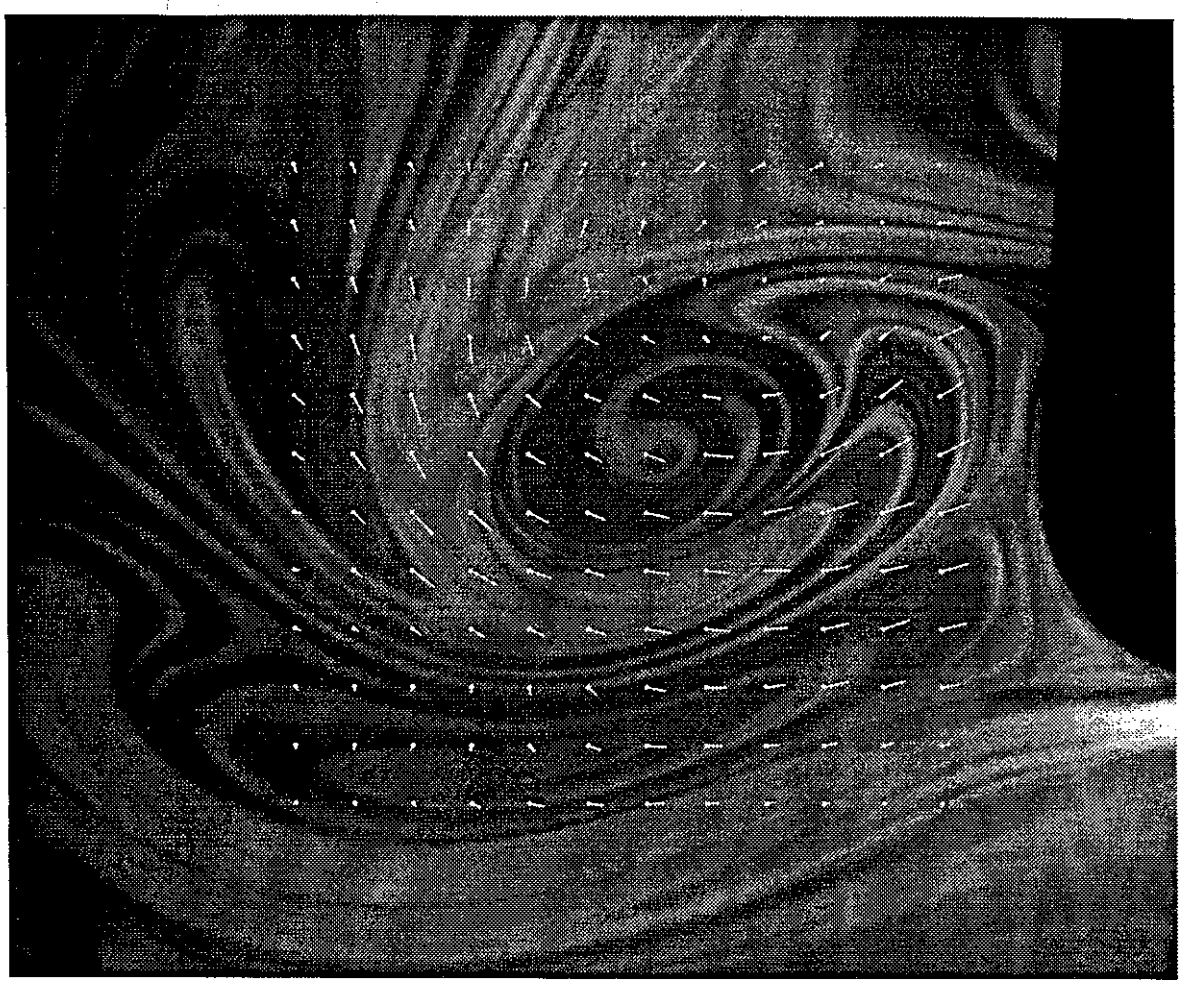

FIG. 11 Displacement of centers of grid over 100 ms.

in Fig. 13, exposes the three-dimensionality in the flow. Figure 14 plots the second invariant of the rate-of-strain tensor. Note the region of strain (rate) that seems to follow the periphery of the large vortical structure. This could be a region of vorticity, from the previously shed vortical structure, that is being strained around the current one.

As a general observation, an important issue arises when imaging a two-dimensional (planar image) slice of a three-dimensional field of a continuous scalar, $c(\mathbf{x},t)$, as in the previous example. An out-of-plane component of the fluid-flow velocity, $\mathbf{u}_f$, coupled with an out-of-plane component of the scalar gradient, $\nabla c(\mathbf{x},t)$, will contribute to the in-plane image-flow velocity $\mathbf{u}$. In this case, the equation for the in-plane image flow can still be written as,

$$\frac{\partial c}{\partial t} + \mathbf{u}\cdot\frac{\partial c}{\partial \mathbf{x}} \equiv \frac{\partial c}{\partial t} + u\frac{\partial c}{\partial x} + v\frac{\partial c}{\partial y} = 0 \ , \tag{50}$$

where we have assumed that the image irradiance $E(\mathbf{x},t)$ is proportional to the two-dimensional slice of the scalar concentration, $c(\mathbf{x},t)$, and where the in-plane image-

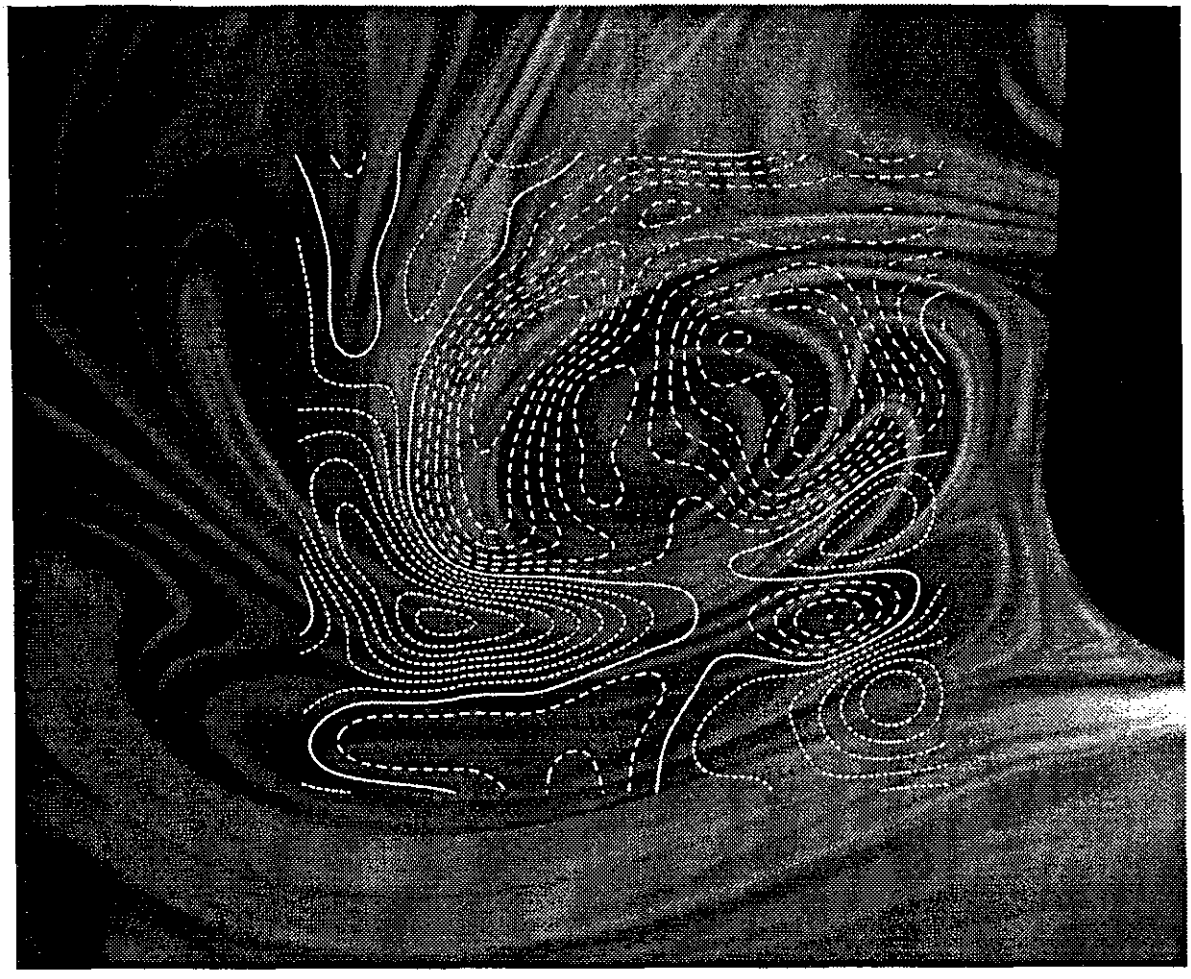

FIG. 12 Contours of constant plane-normal vorticity, $\nabla \times \mathbf{u} = \frac{\partial v}{\partial x} - \frac{\partial u}{\partial y}$. Solid contours denote zero-vorticity. Long dashes denote positive values and short dashes negative. Contours spaced by $0.5\,\mathrm{s}^{-1}$.

flow velocity, $\mathbf{u} = (u, v) = \mathrm{d}\boldsymbol{\xi}/\mathrm{d}t$ (Eq. 11), is the one derived from the minimization function, as described above.

Considering the transport of the three-dimensional iso-scalar surfaces (see Fig. 15), we find that the two-dimensional $\mathbf{u} = (u, v)$ in-plane image-flow velocity components are related to the three-dimensional $\mathbf{u}_\mathrm{f} = (u_\mathrm{f}, v_\mathrm{f}, w_\mathrm{f})$ fluid-flow velocity and the three-dimensional scalar gradient components. In particular, we have,

$$\begin{aligned} u &= u_\mathrm{f} + w_\mathrm{f} \frac{\partial c}{\partial z} \frac{\partial c/\partial x}{(\partial c/\partial x)^2 + (\partial c/\partial y)^2} \,, \\ v &= v_\mathrm{f} + w_\mathrm{f} \frac{\partial c}{\partial z} \frac{\partial c/\partial y}{(\partial c/\partial x)^2 + (\partial c/\partial y)^2} \,. \end{aligned} \tag{51}$$

As can be seen, by substituting Eq. 51 in Eq. 50, these relations recover the three-dimensional transport equation for a conserved scalar field $c(\mathbf{x}, t)$, in the case of

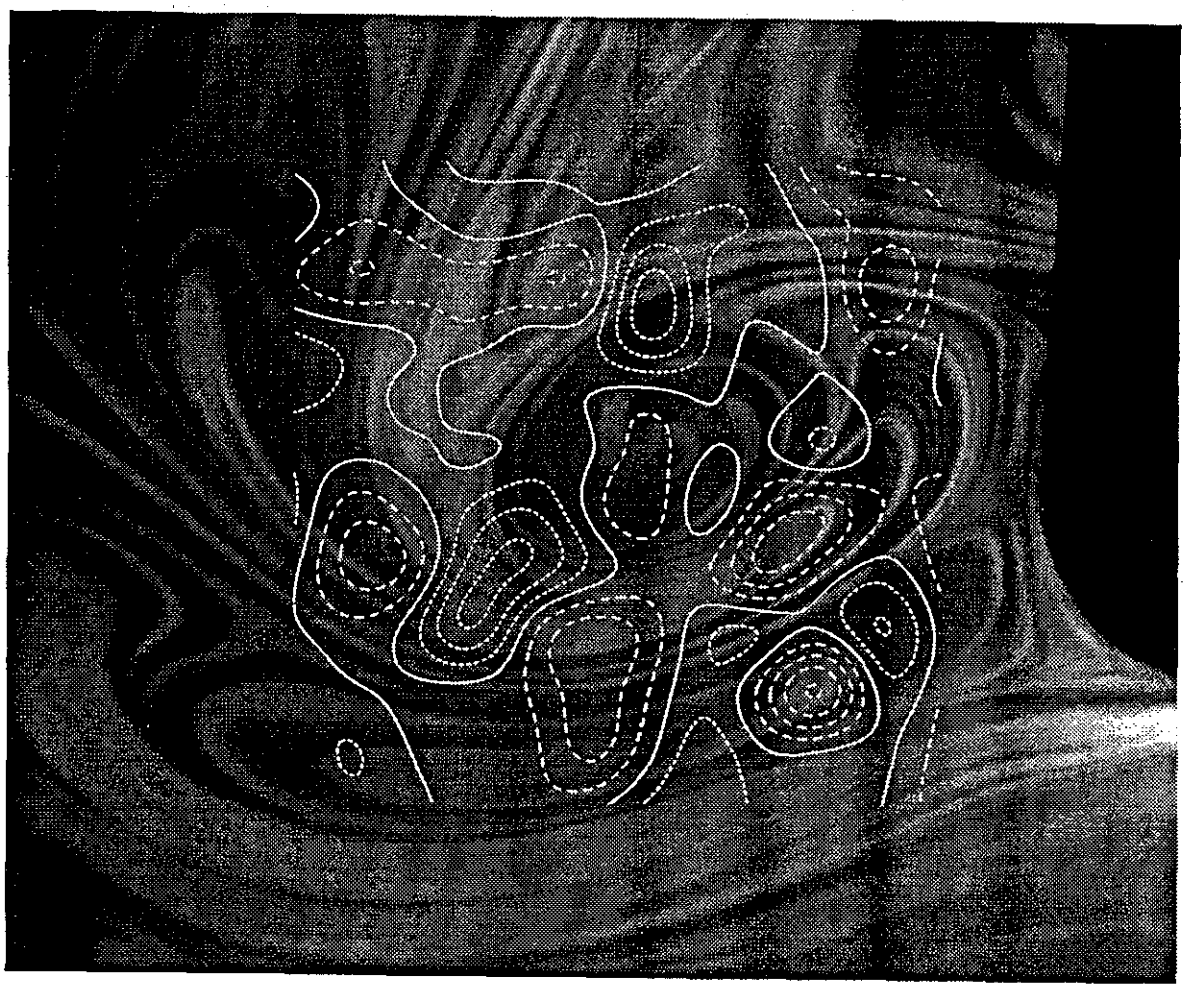

FIG. 13 Contours of constant divergence, $\nabla \cdot \mathbf{u} = \frac{\partial u}{\partial x} + \frac{\partial v}{\partial y}$. As in Fig. 12, the contours are spaced by $0.5\,\mathrm{s}^{-1}$.

negligible diffusion, *i.e.*,

$$\frac{\partial c}{\partial t} + \mathbf{u}_\mathrm{f} \cdot \frac{\partial c}{\partial \mathbf{x}} \equiv \frac{\partial c}{\partial t} + u_\mathrm{f}\frac{\partial c}{\partial x} + v_\mathrm{f}\frac{\partial c}{\partial y} + w_\mathrm{f}\frac{\partial c}{\partial z} = 0 \ .$$

These results provide us with the criteria for when the in-plane image-flow velocity can be regarded as a good approximation to the in-plane fluid-flow velocity. In particular, we will have,

$$u \simeq u_\mathrm{f} \ , \quad \text{if} \quad \frac{u_\mathrm{f}}{w_\mathrm{f}} \gg \left(\frac{\partial c/\partial z}{(\partial c/\partial x)^2 + (\partial c/\partial y)^2} \right) \frac{\partial c}{\partial x} \ , \tag{52a}$$

and

$$v \simeq v_\mathrm{f} \ , \quad \text{if} \quad \frac{v_\mathrm{f}}{w_\mathrm{f}} \gg \left(\frac{\partial c/\partial z}{(\partial c/\partial x)^2 + (\partial c/\partial y)^2} \right) \frac{\partial c}{\partial y} \ . \tag{52b}$$

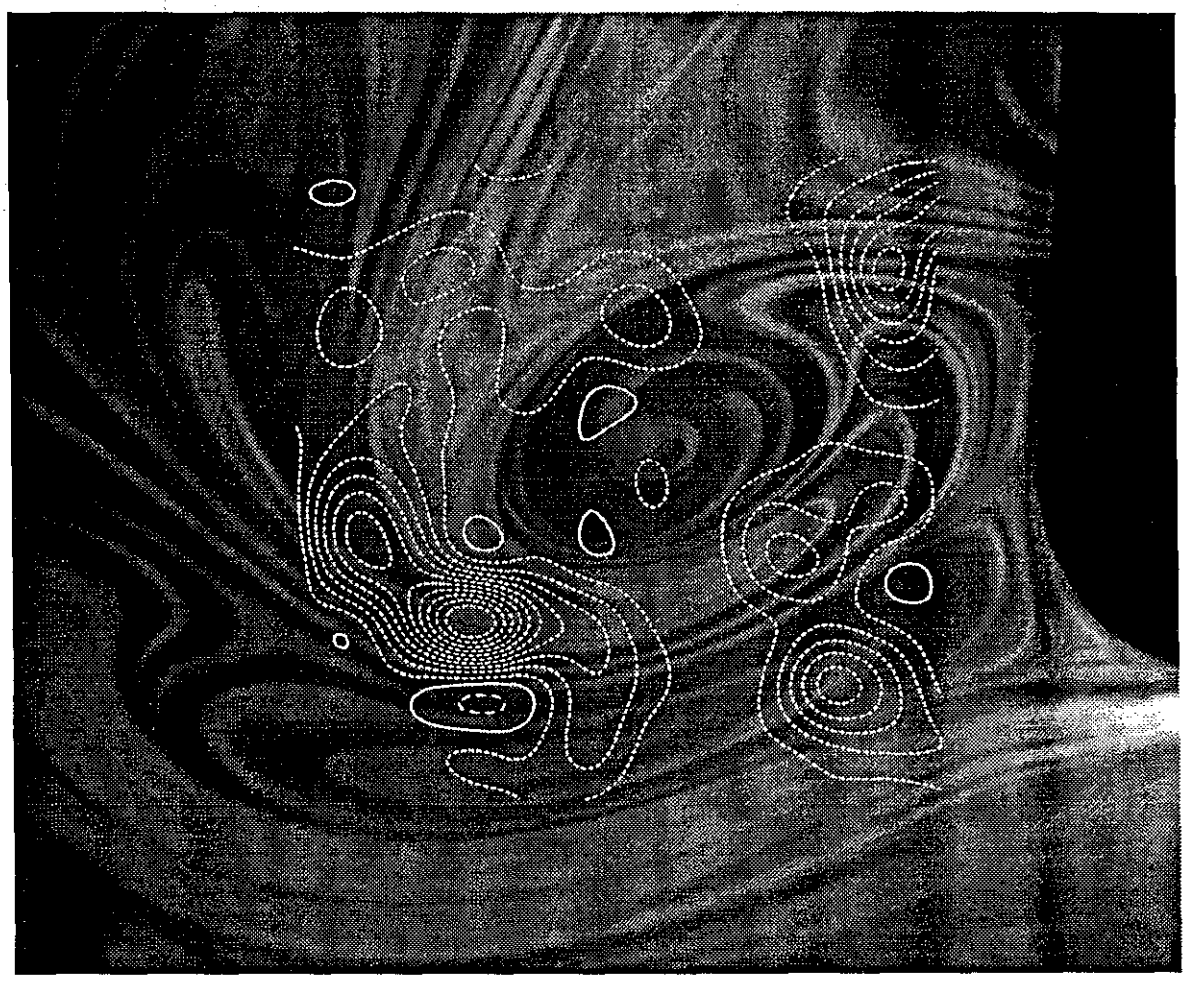

FIG. 14 Contours of constant second invariant of the rate-of-strain tensor (Eq. 45), $q_s = -\frac{1}{2}\left[(\frac{\partial u}{\partial x})^2 + (\frac{\partial v}{\partial y})^2 - \frac{1}{2}(\frac{\partial u}{\partial y} + \frac{\partial v}{\partial x})^2\right]$. Contours spaced by $0.5\,\mathrm{s}^{-2}$.

We can see that if w_f is small, or if $\partial c/\partial z$ is small, or both, by the measure in Eq. 52, then the in-plane image-flow velocity field can be accepted as a good representation of the in-plane fluid-flow velocity field.

Finally, since this method estimates the in-plane image-flow velocity $\mathbf{u}$, and not the fluid-flow velocity $\mathbf{u}_f$, its application to two-dimensional image slices of three-dimensional scalar field data is identical to its application to two-dimensional scalar data.

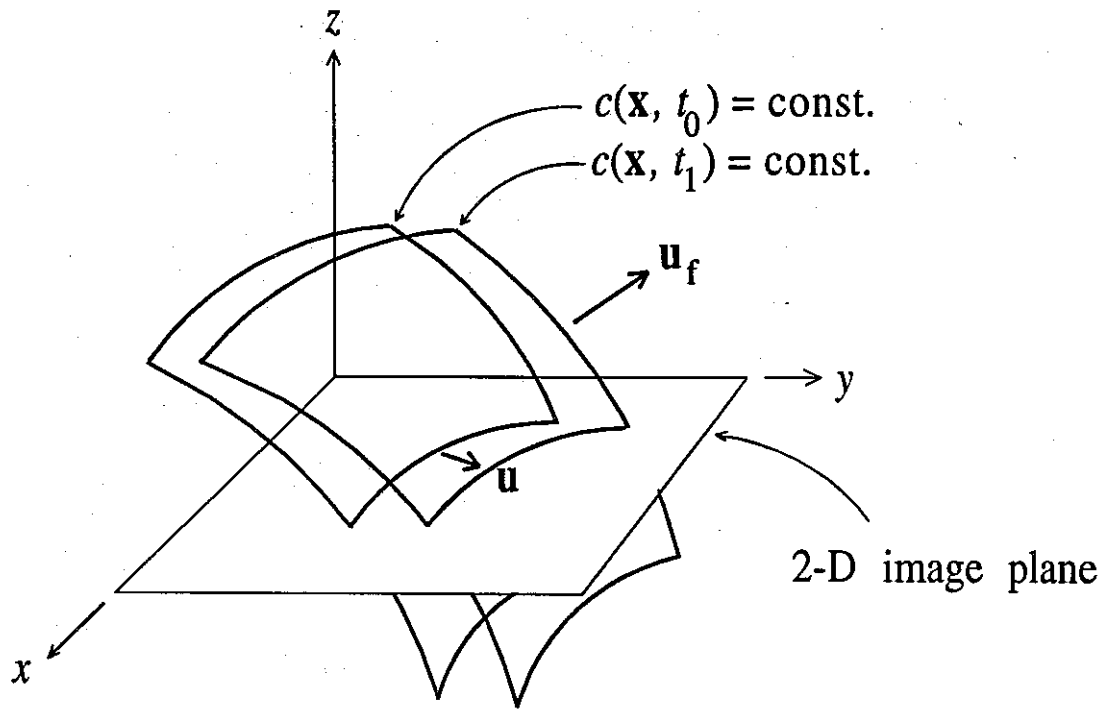

FIG. 15 Two-dimensional slices of a three-dimensional scalar field $c(\mathbf{x}, t)$. $\mathbf{u}_f$ indicates the 3-D fluid-flow velocity and $\mathbf{u}$ is the resulting two-dimensional in-plane image-flow velocity.

5. Voyager 2 images of Jupiter

The method is also illustrated on a pair of the images of the atmospheric dynamics of Jupiter taken by Voyager 2. These images were taken from the "Voyager Time-Lapse, Cylindrical-Projection Jupiter Mosaics," by Avis & Collins (1983). 640 × 350 pixel subimages of rotations 349 and 350 were used in the correlation process. The subimage spans 168° to 97° longitude and 0° to −46° latitude (the equator is at the top of the image). The subimage from rotation 349 is shown in Fig. 16, with an overlay of the initial placement of the correlation volume neighborhoods. The vertical line on the left is a reference line which is to be deformed using the mean zonal velocities of Jupiter from Limaye (1985). Figure 17 shows the same region, one rotation later, with the associated grid deformed by the nonlinear correlation method. On the left is the reference line from Fig. 16, carried by the mean zonal flow. The displacement of the centers of the correlation volumes is shown in Fig. 18.

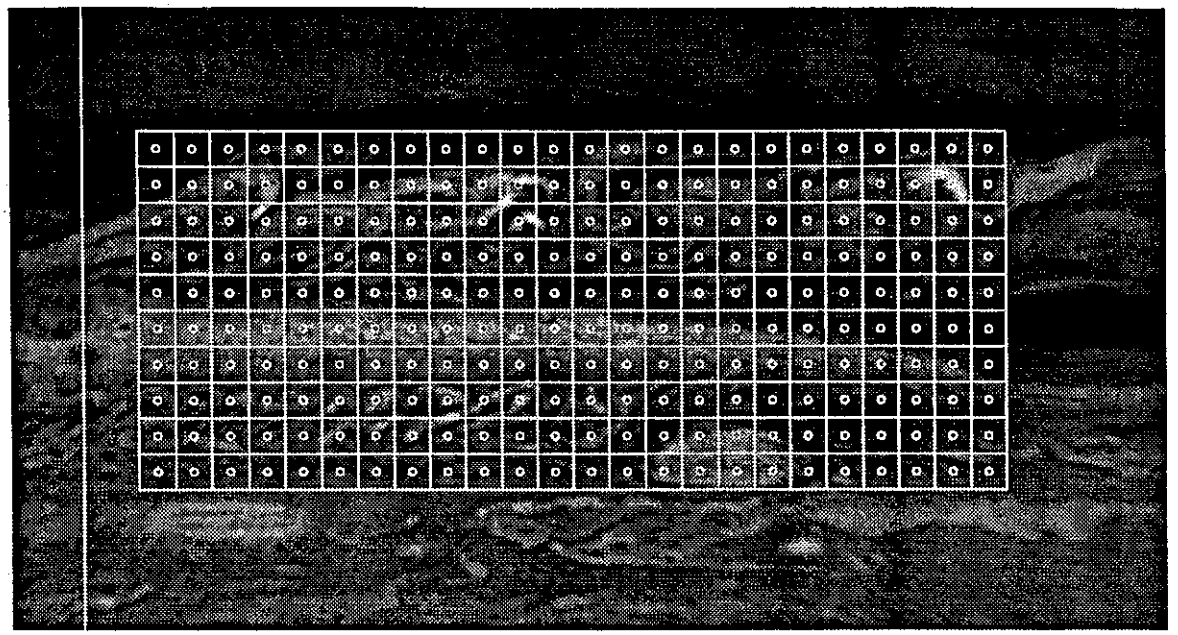

FIG. 16 Initial placement of correlation volumes overlayed on a sub-image of rotation 349 from the "Voyager Time-Lapse, Cylindrical-Projection Jupiter Mosaics." Each square of the grid denotes a correlation volume. The vertical line on the left is a reference line to be carried with the mean zonal velocity of Jupiter (see Fig. 17).

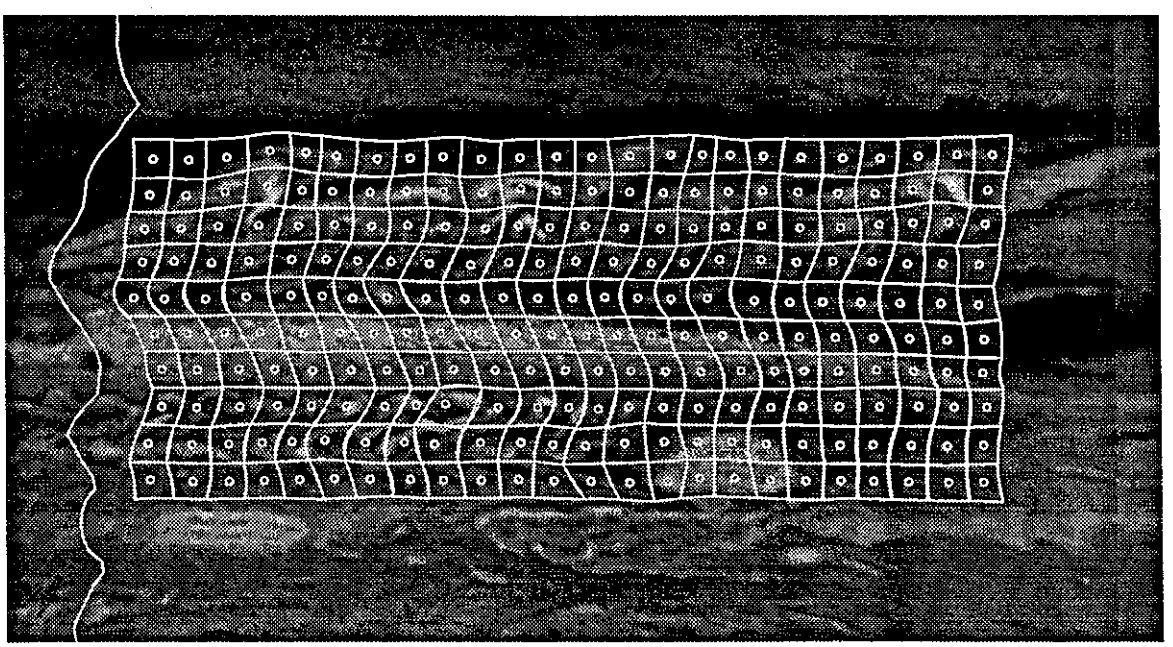

FIG. 17 Deformation of the correlation volumes (see Fig. 16), after one rotation. The line on the left was deformed from the vertical line in Fig. 16 using the mean zonal velocity of Jupiter.

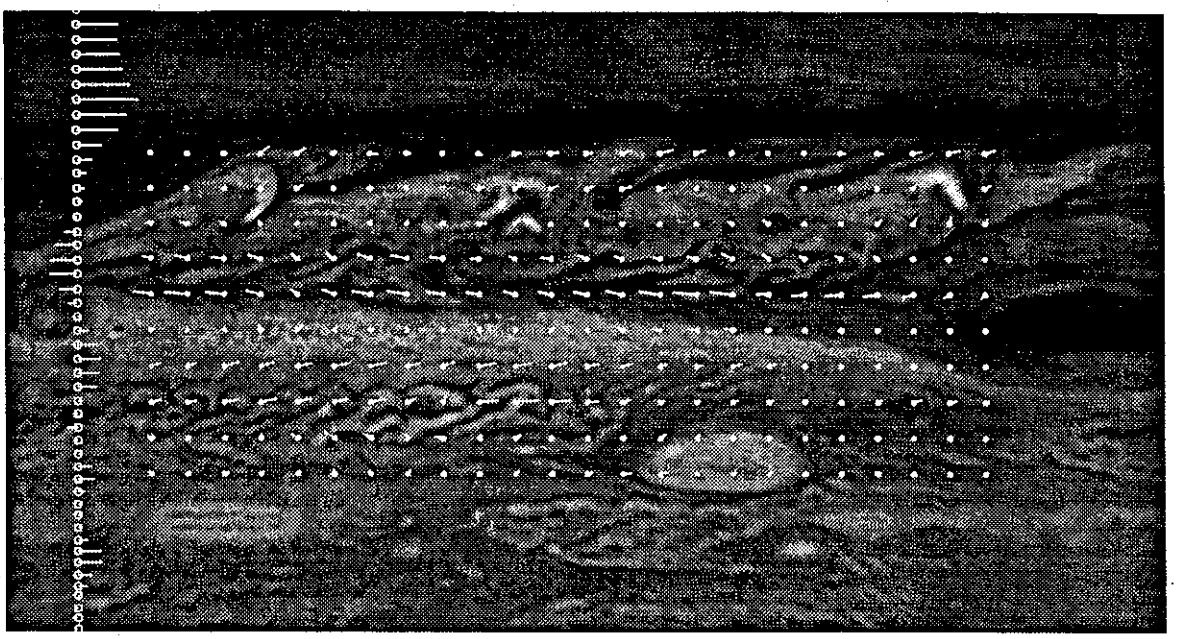

FIG. 18 Displacement of grid control points (centers of correlation volumes) after one rotation. The lines on the left denote the displacement *via* the mean zonal flow of Jupiter.

6. Conclusions

Series expansions of image displacement, in conjunction with a global nonlinear correlation method, can be used to measure fluid velocities, and velocity gradients, from pairs of continuous, convected, scalar images. It is shown that increasing the order of the expansion can improve the accuracy of the results. The proposed method does not require discrete particles and may also be used in situations where there is a natural marker already in the flow, *e.g.*, species concentration can be used to measure velocities in compressible flows. The method is developed for three-dimensional data sets and demonstrated on two-dimensional images of fluid flow.

Acknowledgements

This research was supported by AFOSR Grant Nos. 90-0304 and F49620-92-J-0290, and in a joint contract with M. Gharib of UCSD by DARPA/Navy Grant No. N00014-91-J-1968. We would also like to thank Stewart (Andy) Collins and his group at JPL for their collaboration.

References

ADRIAN, R. J. [1991] "Particle-imaging techniques for experimental fluid mechanics," *Annu. Rev. Fluid Mech.* **23**, 261-304.

AVIS, C. C. and COLLINS, S. A. [1983] "Voyager Time-Lapse, Cylindrical-Projection Mosaics," Report D-541, Jet Propulsion Laboratory, Pasadena, CA.

BINDSCHADLER, R. A. and SCAMBOS, T. A. [1991] "Satellite-Image-Derived Velocity Field of an Antarctic Ice Stream," *Science* **252**, 181-344.

CANTWELL, B. J. [1992] "Exact solution of a restricted Euler equation for the velocity gradient tensor," *Phys. Fluids A* 4 (4), 782-793.

DAHM, W. J. A., SOUTHERLAND, K. B. and BUCH, K. A. [1991] "Direct, high resolution, four-dimensional measurements of the fine scale structure of $Sc \gg 1$ molecular mixing in turbulent flows," *Phys. Fluids A* **3**(5, Pt. 2), 1115–1127.

FALCO, R. E. and CHU, C. C. [1987] "Measurement of two-dimensional fluid dynamic quantities using photochromic grid tracing technique," *SPIE* **814**, 706-710.

HILDRETH, J. and KOCH, C. [1987] "The Analysis of Visual-Motion - from Computational theory to Neuronal Mechanisms," *Ann. Rev. Neur.* **10**(), 477-533.

HORN, B. K. P. and SCHUNCK, B. G. [1981] "Determining Optical Flow," *Artificial intelligence* **17**, 185-203.

HUTCHINSON, J., KOCH, C., LUO, J. and MEAD, C. [1988] "Computing Motion Using Analog and Binary Resistive Networks," *Computer* **21(3)**, 52-63.

LIMAYE, S. S. [1986] "Jupiter: New Estimates of the Mean Zonal Flow at the Cloud Level," *Icarus* **65**, 335-352.

MCNEIL, S. R., PETERS, W. H. and SUTTON, M. A. [1987] "Estimation of stress intensity factor by digital image correlation," *Engineering Fracture Mechanics* **28**(1), 101-112.

MILES, R.B., CONNERS, J.J., MARKOVITZ, E.C., HOWARD, P.J. and ROTH, G. J. [1989] "Instantaneous profiles and turbulence statistics of supersonic free shear layers by Raman excitation plus laser-induced electronic fluorescence (Relief) velocity tagging of oxygen," *Exp. in Fluids* **8**, 17-24.

MURRAY, D. W. and BUXTON, B. F. [1990] *Experiments in the Machine Interpretation of Visual Motion.* (The MIT Press).

PRESS, W. H., FLANNERY, B. P., TEUKOLSKY, A. A. and VETTERLING, W. T. [1986] *Numerical Recipes. The Art of Scientific Computing.* (Cambridge Univ. Press).

ROSENTHAL, S. L. [1990] "Summary of the Special Sessions on Hurricane Hugo 70th Annual Meeting of the American Meteorological Society 4-9 February 1990, Anaheim, California," *Bull. Am. Met. Soc.* **71**(9), 1339-1342.

SCHLICHTING, H., (TR. J. KESTIN) [1978] *Boundary-Layer Theory* (*Seventh Edition*, McGraw-Hill Pub. Co.).

TERZOPOULOS, D. and METAXAS, D. [1991] "Dynamic 3D Models with Local dng Global Deformations: Deformable Superquadratics," *IEEE Trans. on Patt. Anal. and Mach. Int.* **13(7)**, 703-714.

WILLERT, C.E. and GHARIB, M. [1991] "Digital particle image velocimetry," *Exp. in Fluids* **10**, 181-193.